

High Speed Inductive eRPS Sensor Error Reduction Using COMSOL Multiphysics®

Jean-David Wheeler¹, Thierry Chauchard², Franck Nieceron², Patrick Namy¹, Jean-Marc Dedulle¹, Bertrand Varoquie²

1: SIMTEC, 5 rue Félix Poulat, 38000 Grenoble, France

2: CONTINENTAL AUTOMOTIVE France SAS, Av Paul Ourliac - BP 83649, 31036 Toulouse Cedex 1, France

Abstract

Modern electrical vehicle motors require a precise current control over the rotation of the rotor. These motors have high performance, but their control requirement impose a precise knowledge of the rotor angular position. Rotor position sensor (RPS) are traditionally designed using magnets which are dependent of complex supply chains. The present study is dedicated to a magnet-less inductive RPS dedicated to electrical motors (Inductive eRPS), and thus able to provide rotor position at high speed.

The present analysis showcases the design process of a new Inductive eRPS. The design process uses numerical simulation to optimize the sensor accuracy under realistic component assembly conditions. A numerical model is proposed by SIMTEC to investigate different realistic assembly imprecisions. It solves the Maxwell-Ampère equation in the air, the target, and the coils. The magnetic vector potential is used together with the magnetic scalar potential for the sake of efficiency. Thanks to experiments run at CONTINENTAL Automotive, the angular error prediction precision is assessed thoroughly, and the numerical model is validated for industrial use.

Keywords: rotor position sensor, inductive, electrical motor, electromagnetic coupling, misalignment

Introduction

Electric motors have emerged as cornerstones of modern industrial and transportation systems, driving technological advancements in electric vehicles, robotics, renewable energy, and beyond. Ensuring the precise and reliable measurement of angular position within these motors is a critical endeavor, directly impacting their efficiency, stability, and overall operational capabilities. Traditionally, magnet rotor position sensors for electrical motors (eRPS) have played a pivotal role in providing angular position feedback, enabling closed-loop control, and facilitating various motor-driven applications. They are typically precise down to the tenth of a degree and require a simple signal treatment¹. These sensors unfortunately depend on complex supply chains.

Various alternatives have been explored in the past decade. Jerančič et al.² developed and tested an induction sensor, and the coil is printed on a flexible substrate. Although compact, the device has a limited stroke, and the precision of the angle measurement is not sufficient for electric motor rotor application. Zhang et al.³ have proposed and analyzed a rigid device in 2013. The underlying physics principle is also induction. In 2017, Shao published a thesis⁴ on automotive inductive position sensors, revealing a thorough investigation on a set of different designs. The main idea is to measure how a conductive rotor part disturbs an otherwise axially symmetric magnetic field.

Theory

The main idea is to couple two sets of coils on the stator part, and a conducting part on the rotor, called

the target. The target (grey color in Figure 1) presents N identical lobes distributed angularly in the azimuthal plane, perpendicularly to the rotation axis (see Figure 1). The first set of coils is composed of two transmitting coils (TXs, yellow color in Figure 1), whereas the second set is composed of four receiving coils (RXs, blue, green, red and cyan colors in Figure 1). Only one TX and two RXs are used at the same time: the other coils are available for the sake of redundancy. The TX is a classical circular coil, but the RXs present $2*N$ identical lobes distributed angularly in the azimuthal plane. Each RX coil is composed of N clockwise loops, each alternating with one of the N counterclockwise loops. Besides, the two RXs are shifted angularly to one another. The TX emits a signal in the MHz frequency range. This signal is constant and independent of the position of the rotor, but it induces currents in the target. In turn, the target currents emit a signal which is related to the angular position of the target, because of the target lobes. The RXs receive both signals, but the clockwise/counterclockwise architecture cancels the constant part (coming from the TX) and isolates the signal useful for angular position measurement. The first RX delivers a cosine signal (S_{cos}) and the other a sine signal (S_{sin}). The rotor angular position can be obtained by applying the $atan2$ function to S_{sin} and S_{cos} . 4 types of signal imperfections are identified: DC offset, amplitude mismatch, harmonic error and phase shift⁴. An important source of error for the signal imperfections is the stator and rotor misalignments.

The present work investigates the inductive eRPS presented in Figure 1, with $N = 5$ and a coil diameter of approximately 40 mm. The goal is to

assess the influence of misalignments on signal imperfections and its impact on the sensor angular precision.

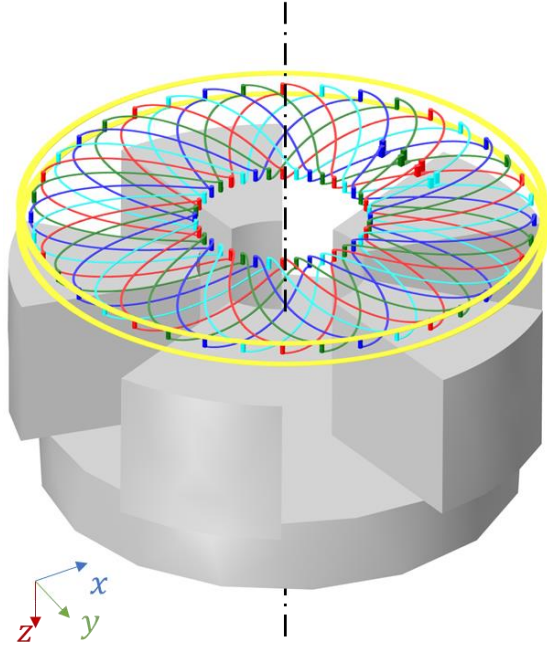


Figure 1. Target (grey), TXs (yellow) and RXs (blue, green, red, and cyan)

Geometry and Misalignments

A fully parametrized geometry model is developed to gather the target and the coils in a single spherical air domain. The misalignment defaults are included in the parametrization to allow for a flexible analysis. The target is built within a cylindrical air domain sharing its axis with the rotation axis (cylinder vertical cut visible as a dashed line rectangle in Figure 4): the cylindrical domain and the target rotate together to account for the rotor motion. The relative motion between the rotating part and the static part is defined by the angle α .

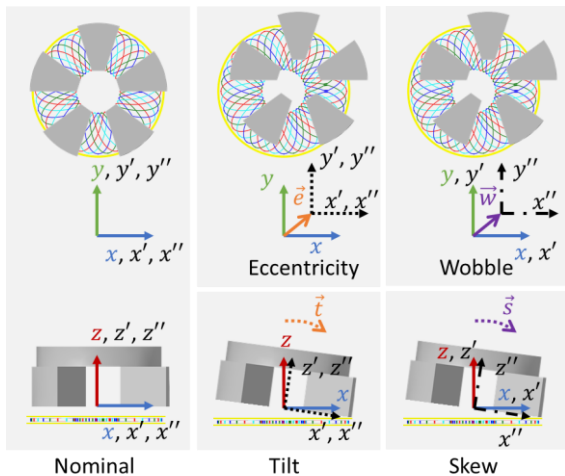


Figure 2. Nominal case together with eccentricity, wobble, tilt, and skew misalignment defaults (default intensity amplified for the sake of clarity)

The linear and angular misalignments are defined in Figure 2 with respectively geometrical frame shifts and rotations. Whereas the fixed frame is defined with color arrows, the *comma* frame is used for the rotation (z' axis being the rotation axis) and the *double comma* frame is used for the target geometry (z'' being the target 5th order symmetry axis). Eccentricity is defined by the vector \vec{e} , wobble by the vector \vec{w} , tilt by the rotation \vec{t} and skew by the rotation \vec{s} . Of course, any combination of the misalignments is also possible.

Experimental setup

The test rig used in this study is CONTINENTAL test bench. (see Figure 3).



Figure 3: Continental test bench

The geometrical precision between the fixed PCB containing the TXs and RXs and the target is of M μm and A $^\circ$. For each test, the target misalignment to investigate is adjusted. Then the target is rotated along a whole 360 $^\circ$ mechanical rotation. The measurement is performed on one of the RXs, according to a 10000 point discretization. One the TXs is emitting its 3.5 MHz signal continuously.

Numerical model

Governing Equations and Boundary Conditions

The electromagnetic field (\vec{E}, \vec{B}) is solved using a frequency domain study in COMSOL Multiphysics[®]. In target and the air surrounding the coils (Domain 1, see Figure 4) Maxwell-Ampère equation ⁵ is solved:

$$\nabla \times \vec{H} = \vec{j}$$

using the magnetic vector potential \vec{A} , with \vec{H} the magnetic field, $\vec{j} = \sigma \vec{E} + j\omega \vec{D}$ the current density, σ the electrical conductivity, \vec{E} the electric field, $\omega = 2\pi f$ the pulsation, f the frequency, and \vec{D} the electric displacement field.

In the rest of the air (Domain 2, see Figure 4), the Maxwell-Gauss equation is solved:

$$\nabla \cdot \vec{B} = 0$$

using the magnetic scalar potential V_m , with \vec{B} the induction field. In Domain 1, one can respectively derive the induction and electric fields:

$$\vec{B} = \nabla \times \vec{A}$$

$$\vec{E} = -j\omega\vec{A} - \nabla V$$

and in Domain 2, the magnetic field is obtained by:

$$\vec{H} = -\nabla V_m$$

The constitutive laws for the induction and electric displacement fields respectively are:

$$\vec{B} = \mu_0\mu_r\vec{H}$$

$$\vec{D} = \epsilon_0\epsilon_r\vec{E}$$

with μ_0 the permeability of the vacuum, μ_r the relative permeability, ϵ_0 the permittivity of the vacuum and ϵ_r the relative permeability. The equations are solved under their 3D harmonic form.

At the junctions between Domain 1 and Domain 2, continuity is imposed between the magnetic vector and magnetic scalar potentials. Domain 2 is divided between the cylindrical domain (composed of the target and the air immediately surrounding it, vertical cut visible as a dashed line rectangle in Figure 4) and a static part (the rest of the magenta domain, which has a spherical shape bounded by infinite element domain). The boundary condition at the outside boundary of the resolution domain is magnetic insulation. Whereas the magnetic vector potential is traditionally used for this kind of topic, the magnetic scalar potential better tolerates the interpolation due to sliding mesh between the rotating part and the static parts of Domain 2.

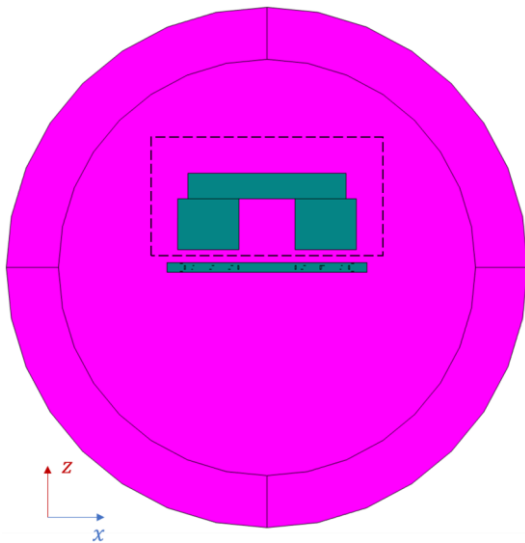


Figure 4. Domain 1 (teal) and Domain 2 (magenta) represented in a cut plane crossing the rotation axis.

Coils

The coils are modelled using the COMSOL Coil feature. The TXs can be accurately represented by a circular homogenized multiturn coil with a voltage of 1V and 3.5 MHz. The RXs are considered as user defined since the lobes and clockwise/ counterclockwise structure is driven by the geometry. They are connected to a 500 kΩ resistor via a circuit to model the hardware impedance.

Mesh

A boundary layer mesh is applied to the target to capture the surface currents according to their skin depth. The triangular mesh at the bottom of the target lobes is 0.5 mm wide. The four RXs are meshed with an identical mesh to minimize the coil voltages differences due to discretization. A fine mesh is applied to both sides of the cylindrical sliding interface, with source to destination mesh size ratio of 1.25 and a mesh of about 0.2 mm. In the infinite element domain, three layers of extruded elements are applied.

Methods

For each misalignment investigated, a full rotation of the target is performed, with a discretization of 1°. This leads to 360 computations for a single misalignment configuration. The voltage at the RX coil terminals is extracted to be post-treated: for each computation, 4 voltages are obtained. To mimic the voltage measurement, the module of the complex voltage value is exported in a spreadsheet for further investigation.

The angle provided by the sensor is computed using *atan2* function and feeding it with a pair of S_{cos} and S_{sin} functions. Both RX pairs are analyzed, the first pair is *Rx1* and the second *Rx2*. Since $N = 5$, the sensor response goes from 0 to 360° within each 0 to 72° mechanical rotation of the target. The former response is called *electrical angle*, whereas the latter is called *mechanical angle*. In the following and unless otherwise specified, *angle* describes the electrical angle. A simple signal treatment based on signal harmonization to equalize the amplitude of both signals and cancel the offset to get the *compensated signal* and the *compensated error* (called *error* in the following). The sensor electrical angle error is set to zero at zero mechanical angle. Electrical angle error is then plotted against mechanical angle. The error peak-to-peak value (or *pkpk*) is also of great interest and is provided together with the graphs.

Simulation and Experimental Results

Nominal case

The nominal case has the geometrical frame, the rotation frame and the target frame all matching at 0° angular position. The target rotation axis is the same as the coil axis. This means that TXs, RXs and target are perfectly aligned. Despite this ideal geometrical situation, each coil provides a voltage with a unique offset (DC component in the signal), sine or cosine unique peak-to-peak amplitude and several harmonics. Whereas the offset can be cancelled, and the amplitude adapted to match the pairing cosine and sine signals, the harmonics remain. Figure 5, upper left graph displays the nominal case angle errors together with the peak-to-peak values for both measurement and numerical prediction. Since the experiment is run using RX2, the numerical data are provided with the same RX unit.

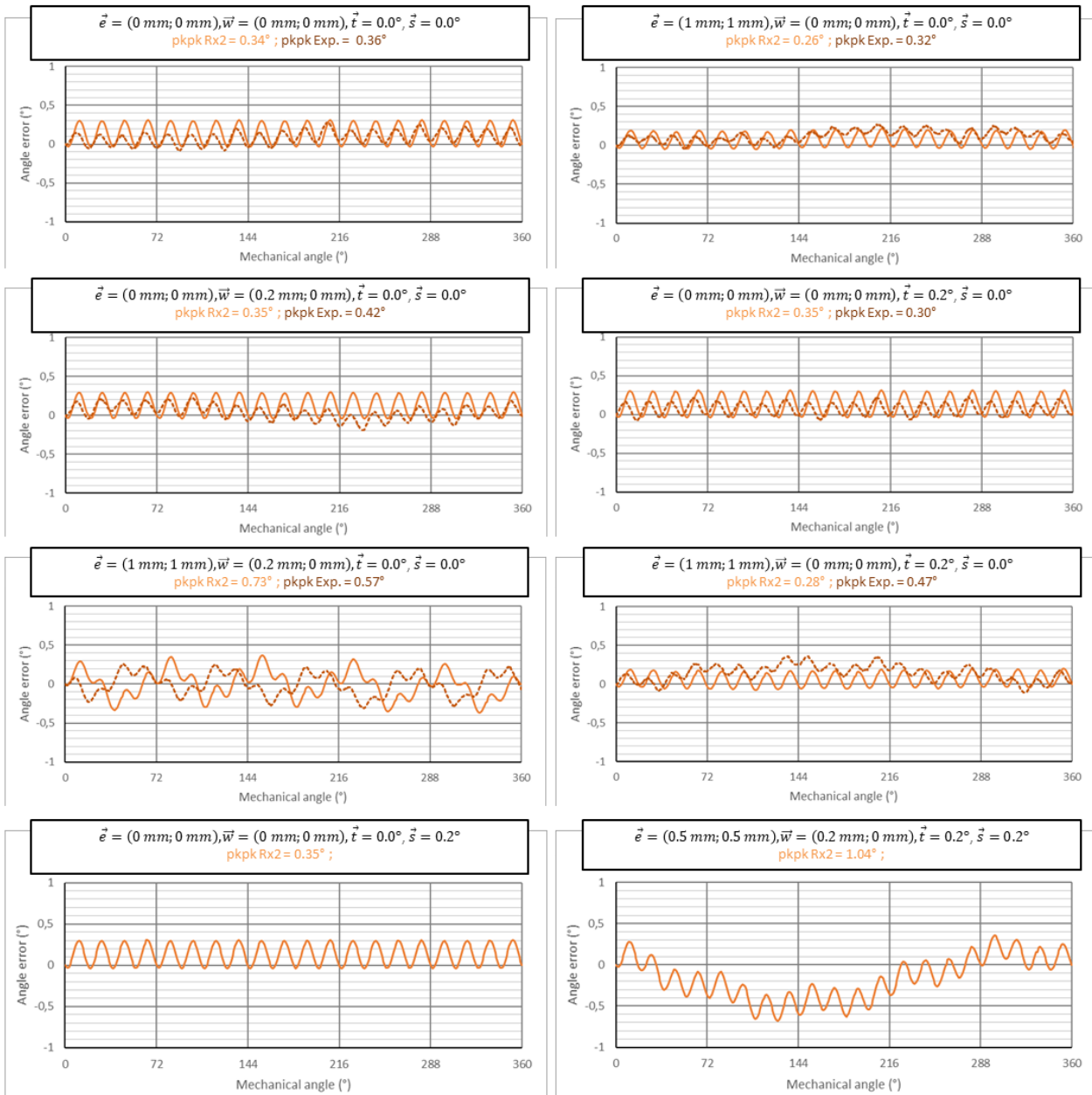


Figure 5. Angle error against mechanical angle for nominal and misalignment cases, together with the peak-to-peak values: comparison between numerical (solid light orange) and experimental (dashed dark orange) results

The graph shows a very good agreement between measurements and numerical prediction. The amplitude of the non-compensable harmonics (period of 18°) differs, but the period matches very well. Although the experimental target has very small fabrication tolerances, a variation appears over the whole mechanical rotation. As a result, the measured peak-to-peak compensated error (0.36°) is very similar to the numerical prediction (0.34°). Both methods confirm that the error is very small. Furthermore, the errors displayed here are errors computed on the electrical angle which runs $N = 5$ times for each mechanical rotation: this means that the mechanical angle error is $N = 5$ times smaller (about 0.07°), which makes the device particularly precise.

Misalignment cases

Despite its geometrical alignment, and as showed above, the nominal case contains inherent angle error. This nominal case is highly idealistic in industrial production world and the misalignments are to be expected. The misalignment amplitudes are defined to be realistic and match achievable industry standards. Eccentricity, wobble, tilt, and skew are individually accounted for in the geometry of the numerical model. The experimental setup was able to reproduce eccentricity, wobble, and tilt, but no target allowed for skew analysis. In addition to the single source misalignment, 3 combinations are explored:

- eccentricity and wobble (exp. + num.),
- eccentricity and tilt (exp. + num.),
- and eccentricity, wobble, and tilt (num. only)

The results are displayed in Figure 5.

Eccentricity errors are plotted against mechanical angle in upper right graph. This specific misalignment, when alone, decreases the angular error compared to the nominal case. More specifically, this default reduces the harmonic error. Both the experiment and the numerical model predict this trend.

According to the numerical model, the wobble, tilt and skew have a similar error to the nominal case. This means that the harmonics are not significantly altered by wobble alone, tilt alone or skew alone. However, the experiment shows slightly different results with the wobble alone and tilt alone since their peak-to-peak errors respectively increase and decrease compared to the nominal case: a variation appears over the whole mechanical rotation and is likely to be caused by small target fabrication error. Finally, when all defaults accumulate, the error is approximately of 1° peak-to-peak ($\sim 0.2^\circ$ pkpk mechanical angle error). This error is particularly small considering the accumulation of realistic misalignment.

When both available, pkpk numerical prediction and pkpk experimental measurement are displayed together in Figure 6. The eccentricity and tilt case present a low-quality agreement between the numerical model and the experiment: it seems that a minor involuntary misalignment was introduced by the experimental setup, with an effect over the whole mechanical rotation. Apart from the combination of eccentricity and tilt (ET in Figure 6), all comparisons show a very similar trend on the pkpk which validates the numerical model as a tool to predict the device measurement behaviour.

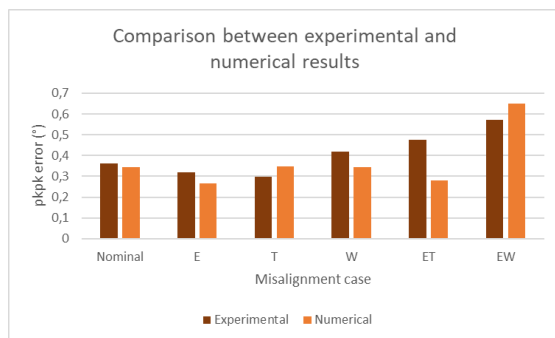


Figure 6. Comparison between experimental and numerical results (E stands for $\vec{e} = (1\text{mm}, 1\text{mm})$, T for $\vec{t} = 0.2^\circ$, W for $\vec{w} = (0.2\text{mm}, 0.0\text{mm})$ while unspecified misalignments are null

Discussion

The several cases investigated show that the device performs well in ideal geometrical configuration and is resilient to realistic misalignments. In the worst-case scenario studied, the electrical angle error predicted is approximately 1° (i.e., mechanical angle error of 0.20°). The configurations explored are representative of the possible real world relative positioning between the target and coils. This range of error is completely acceptable for most

applications. It must be stated that it does not guaranty that the error of any misalignment combination of the same range is below the ones predicted here. Indeed, the coupling between the target and the coil is complex and configuration dependent.

Conclusions

The present study presents a numerical model developed to analyze the precision of a specific eRPS sensor type and a configuration with $N = 5$ is specifically investigated. The sensor performance is predicted in different configurations, including a nominal ideal case and 5 industry realistic cases with geometrical misalignments. The design is proved able to perform with precision for the application of CONTINENTAL customers, especially in an electrical motor control system. Other designs and misalignment configuration can be easily analyzed, using the same numerical model developed by SIMTEC as tool for decision support. Such analysis can be done before the realization of prototypes and expensive experimental testing plan, thus reducing the number of tests to find a suitable design.

References

1. Lemarquand, G. & Lemarquand, V. Annular Magnet Position Sensor. *IEEE Trans. Magn.* **26**, 2041–2043 (1990).
2. Jeranče, N., Vasiljević, D., Samardžić, N. & Stojanović, G. A compact inductive position sensor made by inkjet printing technology on a flexible substrate. *Sensors* **12**, 1288–1298 (2012).
3. Zhang, Z., Ni, F., Dong, Y., Jin, M. & Liu, H. A novel absolute angular position sensor based on electromagnetism. *Sensors Actuators A Phys.* **194**, 196–203 (2013).
4. Shao, L. Automotive Inductive Position Sensor. *Electron. Thesis Diss. Repos.* (2017).
5. Maxwell, J. C. *A Treatise on Electricity and Magnetism : voll.* (Macmillan and co., 1873).